Limnol. Oceanogr., 50(6), 2005, 1787–1794

The optical volume scattering function: Temporal and vertical variability in the water column off the New Jersey coast

Yogesh C. Agrawal[1]
Sequoia Scientific, Inc., 2700 Richards Road, Bellevue, Washington, 98005

Abstract

I present optical data collected offshore of the New Jersey coast at the Long Term Ecological Observatory LEO-15 during the summer of 2001. The data were collected by using a LISST-100 instrument, which measured the volume scattering function (VSF) over the small-angle range 0.1–20° (1.7–340 milliradians) at 670 nm. The measurements only occasionally agree with the widely used data of Petzold. No simple correlation between surface or bottom forcing and the form of the VSF at this site was found. However, a systematic vertical variability as well as a temporal variability in the normalized VSF was observed. In particular, the departure from Petzold's form appears to increase with increasing depth. Power-law forms of the time-averaged small-angle normalized VSF as a function of depth are given.

The volume scattering function (VSF) of water is an inherent optical property that governs the propagation of light below the surface. The small-angle forward VSF is relevant to a particular set of situations in ocean optics, namely, the propagation of laser beams, LIDAR, and image degradation or blurring. The VSF is the sum of three components: VSF of pure water, VSF of particulates, and VSF owing to turbulence (Mobley 1994; Bogucki et al. 1998). In most situations, particulates are the dominant factor, although turbulence can be more important, particularly at small angles and under conditions of severe turbulent microstructure. The contribution owing to turbulence was theoretically modeled by Bogucki et al. (1998). The particulate contribution can be modeled by using Mie theory if particles are assumed to be homogeneous spheres and if particle size distribution and refractive index are known (van de Hulst 1981).

It is useful to consider the influence of particle size on the small-angle VSF. The main forward scattering lobe of particles, as computed by using Mie theory, is nearly identical to diffraction by the particle. The location θ_0 of the first minimum of this lobe is defined by the Airy function such that $ka\theta_0 = 3.83$, where k is $2\pi/\lambda$ and a is particle radius. It follows that VSF at angles greater than, say, 1° excludes the main diffraction lobe of particles of $ka > 218$, or roughly 20-micron radius. Conversely, the dynamics of large particles will affect the shape of the VSF at small angles. In short, particle dynamics, whether through sediment or biological processes, are expected to affect the VSF.

The measurement of the small-angle part of the VSF has been particularly difficult owing to the need to reject the original light beam and scattering from optical surfaces at these same small angles. For this reason, since Petzold's (1972) original pioneering work, no new small-angle data were reported for over two decades, until the work of Lee and Lewis (2003). The new instrument designed by Lee and Lewis (2003) presented glimpses of variability of the small-angle VSF, prompting them to conclude that this variability suggested the need for frequent observations instead of using standard forms. Their instrument reached 0.6° at the low end, and 177.3° at the high end. To achieve this range, the instrument was relatively complex, involving a slowly rotating periscope element. Moored observations with such a device have not been reported to date, probably owing to this complexity. This instrument has also been used to identify bubbles in a surface layer through enhanced scattering in the 60–80° range (Zhang et al. 2002).

The instrument used in the present study was originally developed for particle size distribution measurements (Agrawal and Pottsmith 2000); it measures and inverts the small-angle VSF. The stability of the inversion algorithm requires that the measurements be made at logarithmically increasing angles, and that the angles covered be scaled with the desired particle size-range (Hirleman 1987; Agrawal and Pottsmith 2000). Measurements are made from a fixed geometry, not involving moving parts, over the range 0.1–20° (corresponding to a measurable size range of 1.25–250 microns). Because this instrument does not involve moving components, it consumes little power, which made it possible to make a detailed study of the VSF over a 1-week period from a bottom mounted profiling mooring at the Rutgers University's LEO-15 site (Schofield et al. 2001). The water depth at this site is ~15 m, and power and communication facility are available from a submerged node.

Methods

The VSF $\beta(\theta)$ quantifies how light incident on an elemental volume is scattered in different directions. It is defined as the radiant intensity dI (watts steradian^{-1}, henceforth W sr^{-1}) emanating from an elemental volume dV in a given direction θ per unit incident radiance E (W m^{-2}), i.e.,

[1] Corresponding author (yogi.agrawal@sequoiasci.com).

Acknowledgments

I am indebted to the many people at Rutgers University's Tuckerton Field station who, under the guidance of Prof. Oscar Schofield, exercised the mooring profiler on a 24-h schedule for a full week. Chuck Pottsmith and Doug Keir of Sequoia helped with instrumentation. The profiler was designed at Woods Hole Oceanographic Institution under the direction of Dr. John Trowbridge. I am indebted to two reviewers for effecting very significant improvements to the manuscript. This work was supported by the Office of Naval Research under Contract N00014-02-C-0123.

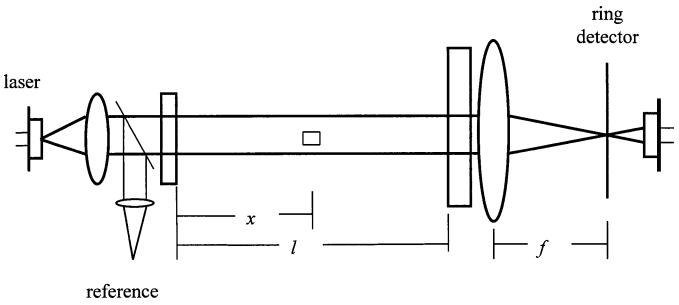

Fig. 1. A diode laser (far left) emits a beam that is collimated. A portion of the beam is split off as a reference measurement. The beam illuminates particles between two flat windows. The direct beam and scattered light is focused by a receive lens. The detector senses multiangle scattering. The photo-diode behind the detector measures optical transmission. An elementary volume is shown at a distance x from the left window. Window separation is l, lens focal length is f.

$$\beta(\theta) = dI/[\mathrm{E}dV] \tag{1}$$

In addition to the VSF, I introduce the scattering coefficient $b(\mathrm{m}^{-1})$ which describes the fraction of total light removed from a beam by scattering:

$$b = 2\pi \int_0^{\pi} \beta \sin(\theta)\, d\theta \tag{2}$$

The *scattering phase function* is defined as β/b and gives information on the shape of the VSF.

Measuring VSF with the LISST-100—The LISST-100 instrument (Sequoia Scientific) consists of a collimated beam derived from a laser diode, a sample volume (6-mm diameter, 5 cm long) that is defined by the water between two pressure-resistant optical windows, and receiving optics that focus the scattered light on a specially constructed multiring detector at the focal plane of a receiving lens, Fig.1. The detector rings are concentric, and their radii increase logarithmically, that is, in a geometric progression. The focused beam passes through a 75-micron hole at the center of the detector rings and is sensed by a photodiode that is placed behind them. The beam-attenuation coefficient c is computed from this optical transmission measurement. The 75-micron pinhole defines an acceptance angle of 0.036°. This small aperture results in estimates of c that are more accurate than those of other systems that typically have this cut off at ~1° and that consequently produce an underestimate of c (Voss and Austin 1993). Slade et al. (2004) reported agreement between Mie theory and measurements with the LISST-100 instrument. All measurements in this article are presented using a 670-nm red laser that was originally built into the LISST instrument.

There are 32 photosensitive silicon rings in the multiring detector. Because of the logarithmic ring radii, the ratio of the outer to inner ring radius of any ring is $(200)^{1/32} = 1.18$, where 200 is the dynamic range of angles, equal to the ratio of the outer diameter of the largest ring, to the inner diameter of the smallest ring. The rapidly increasing area of successively larger rings, combined with rapidly decreasing intensity of light scattering away from center, results in a reduction of the dynamic range of optical power sensed by the detectors. Consequently, only an 8- or 12-bit analog-to-digital converter for recording the photocurrents is sufficient. The detector rings also average over speckle structure, which reduces measurement noise.

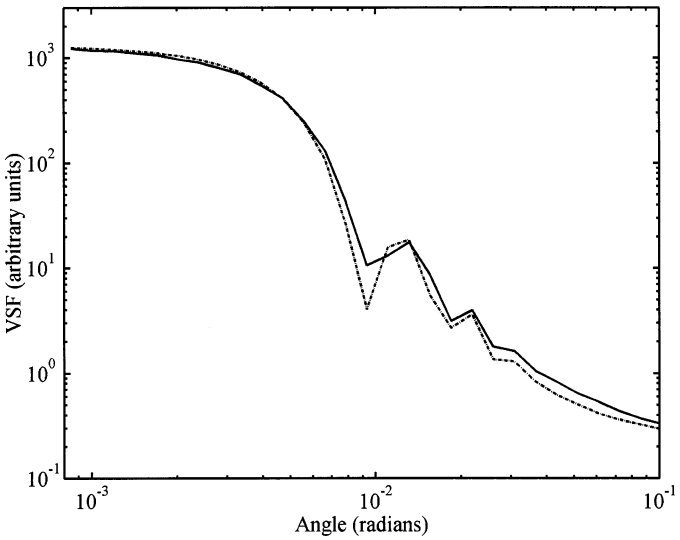

Fig. 2. Comparison of the measured (solid line) and Mie calculation (dotted line) for $ka = 400$, glass spheres in water. For these data $c = 1.4\ \mathrm{m}^{-1}$. Note the absent multilobe structure in the Mie curve. This is due to averaging over the widths of the individual ring-detectors.

Referring to Fig. 1, consider a small length dx of the beam, located at a distance x from the transmit window. For a small area of the laser beam dA, the elementary volume $dV = dA\, dx$. If $\beta(\theta)$ is the VSF, then for laser power P_0 (in watts) entering from the transmit window, and with a beam-attenuation coefficient c (in m^{-1}), by definition of the VSF, Eq. 1, scattered power in any direction will be (Mobley, 1994)

$$dP = e^{-cx}\mathrm{P}_0/\mathrm{A}\beta(\theta)\, dAdxd\Omega \tag{3}$$

where

$$d\Omega = 2\pi\phi\theta d\theta \tag{4}$$

The factor ϕ denotes less than full circle coverage of ring detectors ($\phi = 1/6$ for the present system).

Substituting and integrating, we have the optical power on ring i as

$$\mathrm{P}_i = 2\pi \iiint e^{-cl}(\mathrm{P}_0/A)\beta(\theta)\phi\, dA\, dx\theta\, d\theta \tag{5}$$

An additional attenuation of the scattered light from x to l is included to convert the exponential factor to e^{-cl}. Since the pathlength of the beam between the two windows is only 5 cm, β can be assumed to be independent of the location of the elementary volume. Furthermore, the VSF is assumed to be a slowly varying function of angle over the width of a single ring detector, so that we use its *mean* value $\boldsymbol{\beta}_i$ over each of the 32 angle subranges represented by the ring de-

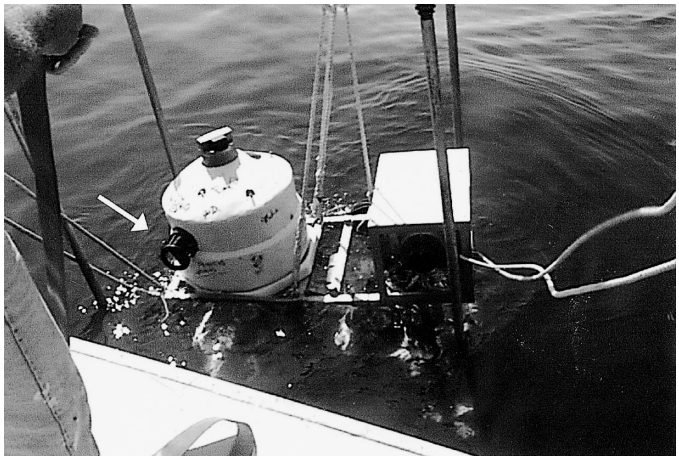

Fig. 3. The LISST-100 on the profiler is shown with an arrow. The sample volume is located outside the protective white cylindrical dome.

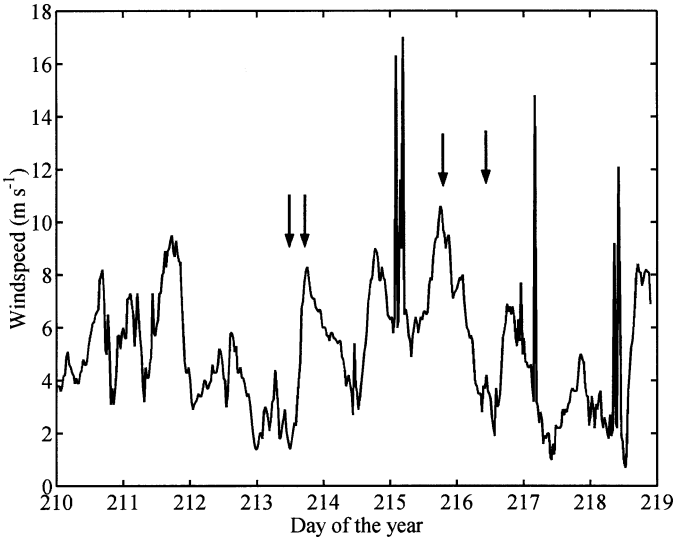

Fig. 4. Wind speed (m s^{-1}) covering the duration 29 July–8 August 2001. Arrow pairs indicate two events; first a spin up, and second a spin down.

tectors. This is a reasonable approximation because, even at the steepest part of the VSF, the smallest ring detector covers the angle range 0.1–0.118°, over which Petzold's measurements suggest <25% variation. Integrating Eq. 5 over $x = 0$ to l gives the power sensed by ring i as

$$\mathrm{P}_i = \pi e^{-cl} l \mathrm{P}_0 \boldsymbol{\beta}_i(\theta) \phi(\theta_{i+1}^2 - \theta_i^2) \tag{6}$$

When laboratory data are collected with filtered, particle-free water, Eq. 6 takes the form

$$\mathrm{P}_{i,w} = \pi \exp(-c_w l) l \mathrm{P}_0 \boldsymbol{\beta}_{i,w}(\theta) \phi(\theta_{i+1}^2 - \theta_i^2) \tag{7}$$

where the subscript w denotes pure water alone. The corresponding attenuated beam power $\mathrm{P}_{t,0}$ measured by the transmission sensor is

$$\mathrm{P}_{t,0} = \mathrm{P}_0 \exp(-c_w l) \tag{8}$$

When measurements are made in the presence of particles, the transmitted power P_t is

$$\mathrm{P}_t = \mathrm{P}_0 \exp[-(c_w + c_p) l] \tag{9}$$

where the subscript p denotes particles, and we are ignoring the attenuation owing to dissolved organic matter. The optical transmission, τ, is Eq. 9 divided by eight, giving beam attenuation owing to only particles:

$$\tau = \exp(-c_p l) \tag{10}$$

It follows from the difference of Eq. 6 and 7, and noting that $\boldsymbol{\beta}_i = \boldsymbol{\beta}_{i,w} + \boldsymbol{\beta}_{i,p}$

$$\mathrm{P}_{i,p} = \mathrm{P}_i/\tau - \mathrm{P}_{i,w} \tag{11}$$

$$= \pi \exp(-c_w l) l \mathrm{P}_0 \beta_{i,p}(\theta) \phi(\theta_{i+1}^2 - \theta_i^2) \tag{12}$$

Equation 12 shows that the measured quantities P_i, τ, and $\mathrm{P}_{i,w}$ provide a direct measure of the VSF owing to particles alone (ignoring turbulence), after removing contributions from water.

If ρ represents the ratio of the outer to inner radius of any ring, (1.18, noted earlier) then for the ring i which covers angles between θ_i to θ_{i+1}

$$\theta_i = \rho^{i-1} \theta_{min} \tag{13}$$

so that, after substitution, we have

$$\boldsymbol{\beta}_{i,p}(\theta) = [\mathrm{P}_{i,p}/\mathrm{P}_0]\, e^{c_w l}/[\pi \phi l (1 - \rho^{-2}) \rho^{2i} \theta_{min}^2] \tag{14}$$

This is the essential relationship between the power sensed by each silicon ring detector i and the VSF averaged over it, $\boldsymbol{\beta}_{i,p}$. Only three quantities need be measured for each estimate of the VSF: the attenuation τ, which is common to all angles; the laser power entering water P_0; and the power sensed by each ring P_i. As Eq. 14 involves a ratio of optical powers $\mathrm{P}_{i,p}/\mathrm{P}_0$, temperature-related drifts in photo-detection are cancelled out.

In the LISST-100 instrument, the power incident on the silicon rings P_i is converted to electrical current with a nominal radiant sensitivity of 0.47 amperes per watt (A W^{-1}) traceable to the National Institute of Standards and Technology (NIST). The photo-current is converted to a voltage using a current-to-voltage amplifier, with a 1 MΩ feedback resistor giving a sensitivity of 1 volt per microampere (V μA^{-1}). The consequent overall radiant sensitivity is 0.47 V μW^{-1} of optical power. The photocurrent is digitized with a 12-bit analog to digital converter. Therefore, each digital count of the data represents 5 V per 4096 counts, i.e., 1.22 mV count^{-1}. It follows that one digital count corresponds to 2.596 nW optical power. If N_i is the number of digital counts recorded for ring i, then $\mathrm{P}_i = 2.596 \times 10^{-9} N_i$ watts.

The laser power P_0 entering the water at any time is corrected for drift at a later time. P_0 at any time is determined by multiplying the output of the laser reference sensor with a factor ζ, which is the ratio of the laser power P_0 entering the water (in watts), as measured with an NIST traceable laser power meter, and the laser reference output N_r (in digital counts) during laboratory testing, i.e., $\mathrm{P}_0 = \zeta\, \mathrm{N}_r$. Substituting, we have

$$\beta_i(\theta) = 2.596 \times 10^{-9} N_i / \{\tau \zeta N_r [\pi \phi l (1 - \rho^{-2}) \rho^{2i} \theta_{\min}^2]\} \tag{15}$$

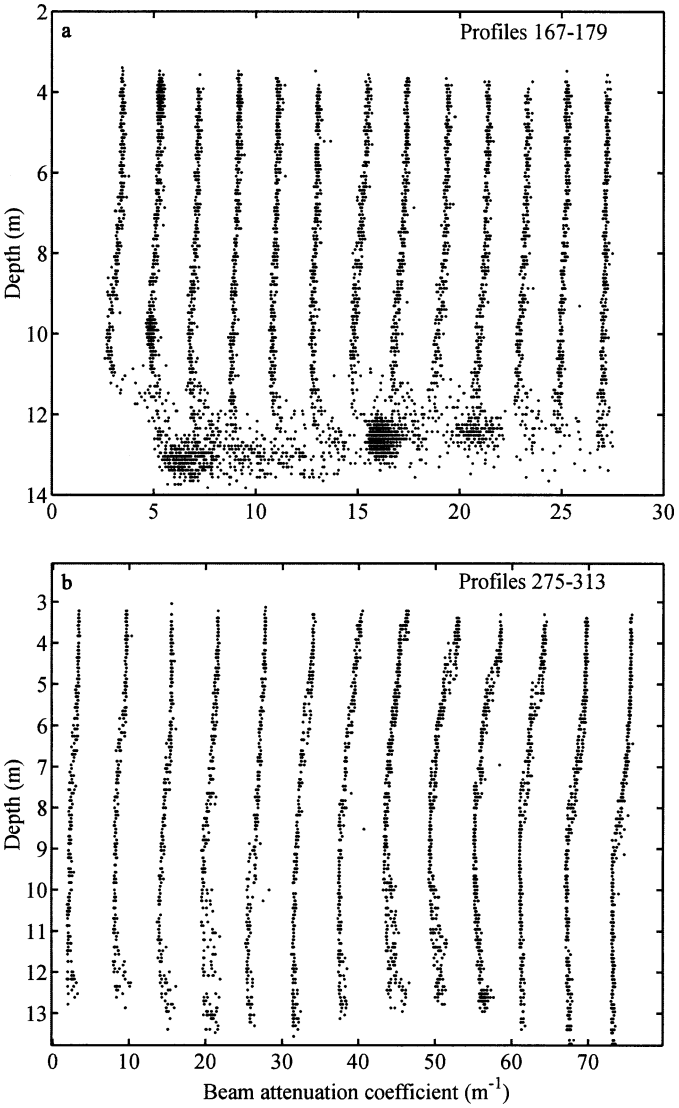

Fig. 5. Profiles of the beam-attenuation coefficient c observed for the two events marked by pairs of arrows in Fig. 4. (a) Profiles 167–179. (b) Profiles 275–313. For clarity, only every third profile is displayed.

This is the final form of the VSF averaged over each ring detector i, as a function of the measured digital counts of light scattering. The quantity in the square brackets is a set of constant factors for the measured values of digital counts from each of the rings, N_i. To convert the VSF to the phase function, an estimate of b is required. Because the LISST-100 instrument does not measure b, we have instead used c_p, Eq. 10, thus producing a *normalized* VSF. This normalized VSF is also reported by Lee and Lewis (2003) and is quite similar to the phase function.

Two tests were performed to ensure the overall accuracy of measurements. First, by using nonabsorbing large particles ($a \gg \lambda$), the total amount of light detected by the ring detectors, $\Sigma_i P_{i,p}/\phi$, see Eq. 12, corrected for 1/6th azimuthal coverage, was compared against measured c_p. This total scattering represents the portion of b covering 0.1–20°, $b_{0.1-20}$. The ratio $b_{0.1-20}/b$ takes values ranging from 0.7–0.8 for nonabsorbing spheres of diameters 2–200 microns and index 1.5 in water, as estimated from Mie theory. This ratio is also near unity for Petzold's data. Thus, the measured ratio $b_{0.1-20}/c_p$ for nonabsorbing large particles should also be near unity. This served as an approximate confirmation of the overall conversion from measurement to VSF. Second, for a more direct cross-check of conversion of digital data in counts to VSF in units m^{-1}, the estimate of $b_{0.1-20}$ was compared to values derived from integrating VSF by using Eq. 2, thus further confirming the transformation from Eq. 15.

As an example of the fidelity of the measurement, in Fig. 2 we show a comparison of Mie theory with laboratory scattering data from 40-micron white PVC particles of refractive index 1.5. Note, first, that the theoretical Mie curve appears different from the familiar multilobe form. This is because the logarithmically widening detector rings integrate the higher-order oscillations of Mie scattering; only the first two lobes can be seen. The logarithmic spacing ensures that the main and secondary diffraction lobes of *any* particle within the measurable size range of this instrument are distinguishable in the measured VSF. Second, the small but finite width of the size distribution of the particles used for this test explains the slightly weaker minima of the measurements. The agreement between Mie theory and data is good.

Auxiliary measurements—The LISST-100 instrument was part of a package installed on a profiler, Fig. 3. The profiler was powered from the underwater node at LEO-15. Data were piped through the node to the shore station at Tuckerton, New Jersey. The profiler was operated remotely, under manual control from Tuckerton, requiring 24-h presence of operators. Depth of the profiler was measured by a pressure sensor that is integral to the LISST-100, and whose output is recorded with light scattering data. The Rutgers University facility maintains a meteorology tower that records wind at two elevations. These data are employed in the present study.

Data processing—The removal of background light originating on optical surfaces on to the ring detectors and correction for drifts in laser output are described in detail by Agrawal and Pottsmith (2000). Briefly, a filtered water measurement is made before the field experiment. The amount of light seen by the detectors constitutes the background, which has been called *zscat* (from zero scatterers). In the field data, the total scattering that includes background and the contribution from suspended particles is first deattenuated by the measured beam-attenuation τ (Eq. 11). Subtracting the background at this stage leaves the particle scattering in digital counts (Eq. 12). The beam-attenuation itself is measured by the ratio of in situ laser transmitted power as sensed by the detector behind the ring-detector array, and laser power entering water, which is determined from the recorded reference laser sensor, ζN_r. A special correction was necessary for ring detectors numbered 5 and 6 for this old model instrument. In this pre-2001 detector, a flaw in the silicon chip rendered these sensors nonlinear. The data presented in this article replace these two detectors with their interpolated value. For this interpolation, I used a second order polynomial fitting rings 2–3 and 7–8. It was not necessary in pro-

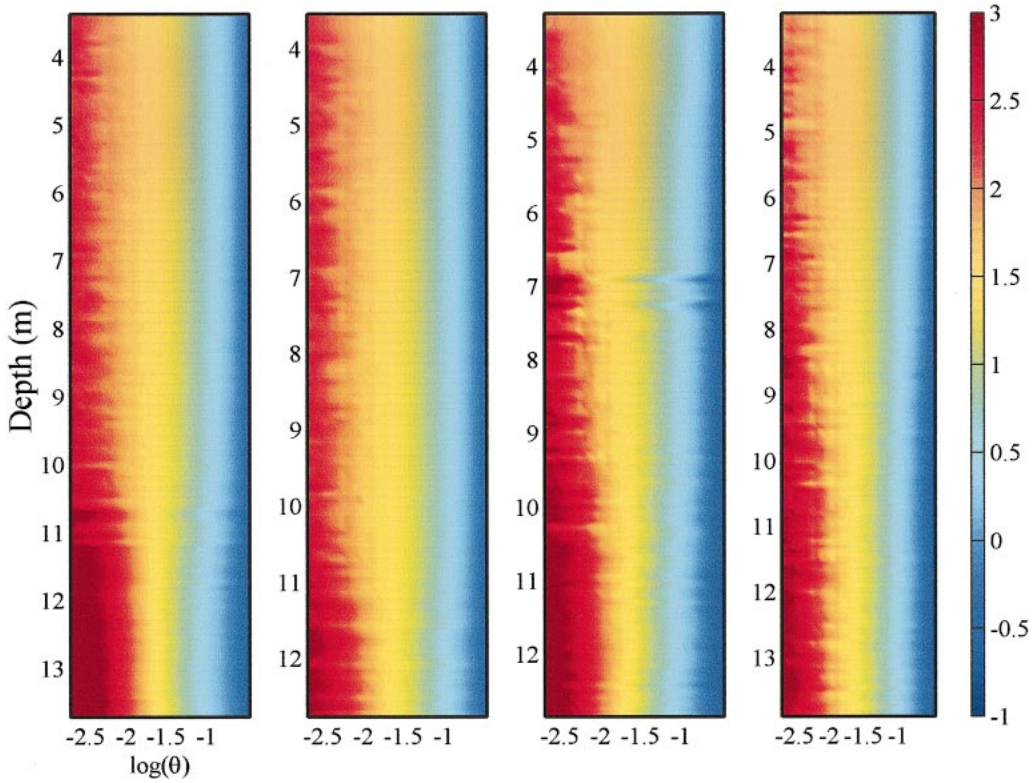

Fig. 6. The normalized volume scattering function versus log of scattering angle and depth. The four profiles displayed are, from left to right, profiles 167, 179, 302, and 313. The corresponding vertical profile of optical transmission for each is included in Fig. 5*a* and 5*b*. The color bar on right defines $log_{10}(\beta)$.

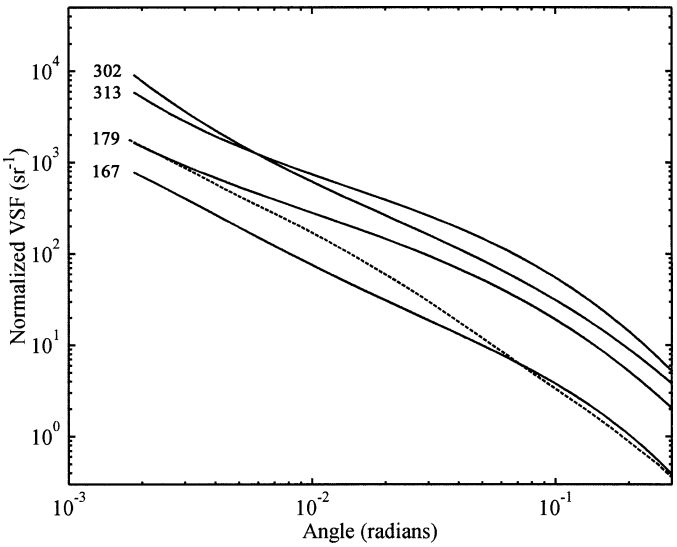

Fig. 7. The mean normalized VSF for the top 9 m of the four profiles shown in Fig. 6. The curves are identified by profile numbers 167, 179, 302, and 313. Curves 179, 302, and 313 are each displaced up by factor of five from previous for clarity. Petzold's data are shown as broken line, undisplaced.

cessing these data to discard any spikes. In contrast with a 1-m path used by Petzold and a 20-cm path used by Lee and Lewis (2003), the smaller path length of the LISST-100 reduces the probability of large particles occurring in the beam, potentially producing more pronounced spiking owing to small number statistics. However, as there are a large number of measurements at any depth, averaging over depth or time achieves smoothing of the effects of spiking.

From the net light scattering in digital counts, and after the correction for rings 5–6, the VSF is obtained from Eq. 15. At this point, the units of VSF are $m^{-1}sr^{-1}$. The normalized VSF (sr^{-1}) is obtained by division by *c*.

Results

Wind speed—Four hundred vertical profiles of the VSF were made covering the period 00:00 h 29 July–00:00 h 6 August 2001. Each profile consisted of 300–400 VSFs, depending on how much of the water column was covered and at what speed. In all cases, beam-attenuation profiles reveal two distinct regions: a surface layer and a bottom nepheloid layer.

During the week of profiler operation, wind conditions varied widely, as did the water column properties, ranging from a classic bottom nepheloid layer with a clearer upper water column, to a clear bottom layer and a well-defined turbid surface layer. Complex mixing patterns resulted from the two wind events. The first began half way into day 213

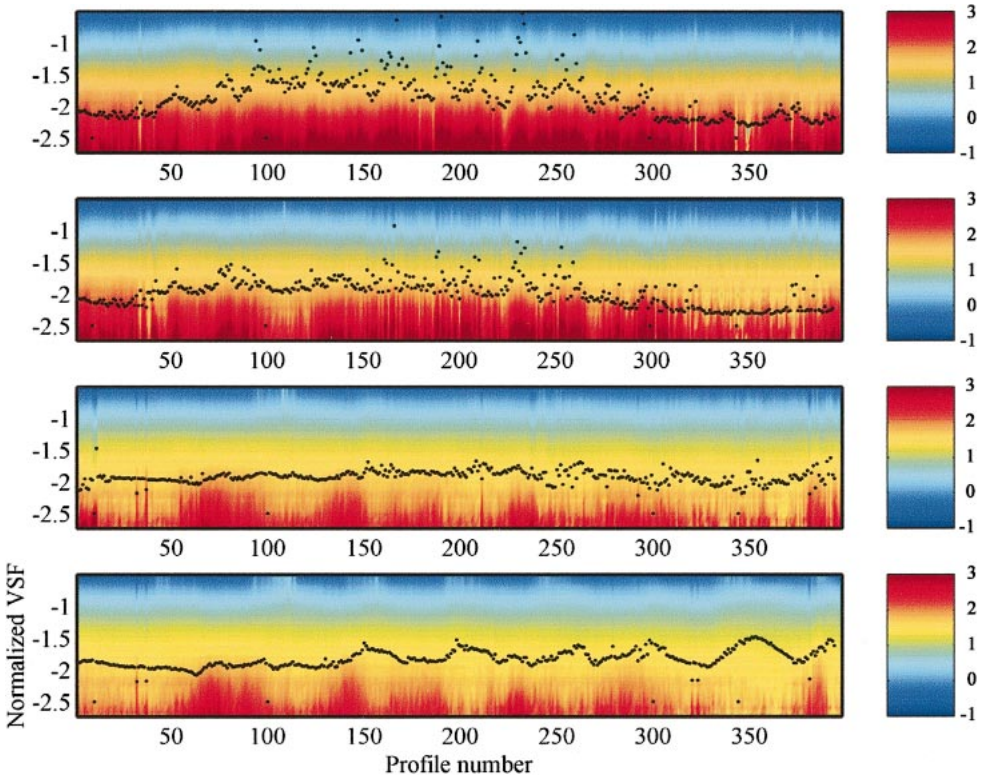

Fig. 8. Time series of the normalized VSF at four depths covering the entire week-long duration. From top to bottom panels, depth is 2, 4, 6, and 8 m. Beam-attenuation coefficient c is overlaid (dots) as $[(0.2 \times c) - 2.5]$. Note steady smoothing of c with increasing depth. The color bar on right defines $log_{10}(\beta)$.

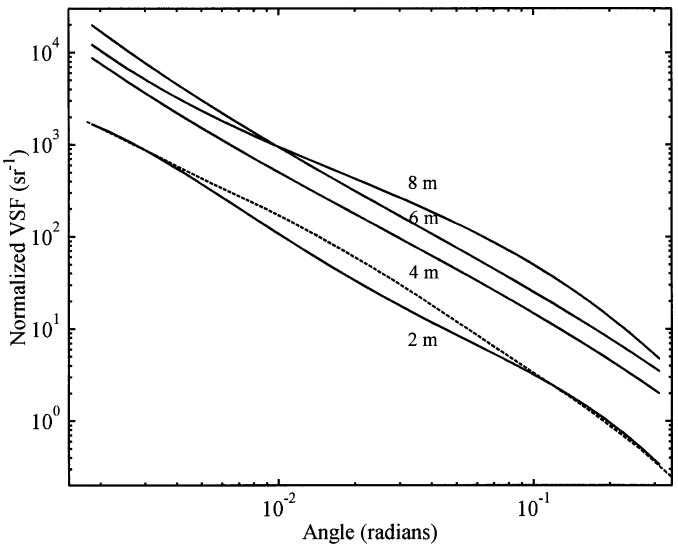

Fig. 9. Normalized VSF averaged over the entire 8-d duration, for the four depths in Fig. 8, along with Petzold's data (dashed line). Again, the curves for 4, 6, and 8 m are each displaced up by a factor of five from previous for clarity.

and ended the same day; the second began mid day 215 and ended a day later (Fig. 4). In the first, speed increased rapidly from less than 2 m s^{-1} to 8 m s^{-1}, representing a ~16-fold increase in surface wind-stress, which produced strong vertical mixing from the surface downward. The second event was a decrease of wind-speed from 10 m s^{-1} to less than 2 m s^{-1}. The resulting relaxation of surface stress permitted midcolumn and bottom processes to dominate during the period.

Optical transmission in the water column—The beam-attenuation coefficient profiles for the two events are shown in Fig. 5. Each successive profile is shifted horizontally by 2 m^{-1} for clarity. In the first event, a weak bottom layer appears to be erased, being replaced by a top-to-bottom mixed layer, which is consistent with the expected effect of strong surface wind stress. The profiler clearly did not fully penetrate the bottom boundary layer, but it is seen that the bottom nepheloid layer was reduced in thickness, eventually being thinner than the deepest penetration of the profiler (we estimate about bottom 2 m of water column was not sampled). At the end of the event, the water column is well mixed, as indicated by a uniform profile. In the second event, the relaxation of wind stress was accompanied by a deepening of the turbid surface layer, which is contrary to expectations of local dynamics. Because beam attenuation is the net effect of light attenuation by all sizes of particles that are present, a uniform profile of c implies that the predom-

inant light-attenuating particles are well mixed, although gradients in smaller concentrations of particles that do not produce much attenuation (e.g., large diameter particles or flocs) may be present. The data show many cases in which large particles are indeed present, which produce individual spikes in optical transmission and an accompanying scattering signature. These spikes are not considered further.

In contrast to the first event, the second (spin-down) event, Fig. 5b, resulted in the establishment of two distinct turbid layers: a well-mixed turbid surface layer overlaying a well-mixed clearer bottom layer that extended up to approximately mid-column height. The structure of the water column is obviously not recognizable in simple terms of local dynamics of bottom or surface resuspension/settling.

Normalized VSF, 0.1 to 20 degrees—As each data point on the beam-attenuation profiles of Fig. 5 accompanies a VSF, it is not possible to display the nearly 2×10^4 VSF observations just during these two events. For this reason, only a few VSF profiles can be considered in detail.

Figure 6 shows the vertical profiles of the normalized VSF for four cases: the beginning and end of the two events shown in Fig. 4. From left to right, the first panel shows a clear-water surface layer overlying a turbid bottom nepheloid layer with a much steeper normalized VSF at the small-angle end. The second and fourth panels show a generally uniform upper column VSF, whereas the third panel shows a gradual steepening of the normalized VSF with depth. These forms are next averaged over the top 9 m, which is a level chosen to avoid the bottom turbid layer that lies below this level for these cases. The resulting averaged forms are shown in Fig. 7. Here, the averaged normalized VSF have been smoothed with a third-order polynomial to remove instrument noise. It is clear that the four surface-averaged normalized VSFs are quite distinct from each other and also from the Petzold phase function (derived from Mobley, 1994 and truncated to 20°). The data suggest that the use of a single standard form for the phase function is not reasonable in this environment.

Figure 8 shows the temporal variation of the normalized VSF at depths of 2, 4, 6, and 8 m only, avoiding the bottom boundary layer region. Data at depths of <2 m are discarded owing to ambient light interference. The normalized VSF shows increasing variability with depth. For example, there is pronounced evidence of a quasiperiodic steepening and flattening of the form at small angles at the 6- and 8-m levels. Overlaid on these panels is the beam-attenuation coefficient c. There is not a strong correlation between variations in the normalized VSF and the beam attenuation, which is consistent with the underlying physics: the two quantities, c and normalized VSF, depend on different properties of the particle population. The absence of this correlation between c and the shape of the VSF means that c can not be used to estimate the normalized VSF. In this coastal environment, a single form of the scattering phase function can not be used.

Figure 9 shows the time-averaged normalized VSF for the four depths of Fig. 8, along with the Petzold form. The vertical trend shows a flattening of the small-angle part of the VSF with depth. Only the surface 2-m form corresponds with the Petzold form. This is further indication of the need to include vertical dependence of the phase function in modeling light propagation at this site.

Table 1. Polynomial coefficients describing mean normalized VSF at 2, 4, 6, and 8 m contrasted with Petzold's data.

Depth	$-a_o$	$-a_1$	$-a_2$
2 m	3.99	2.58	0.23
4 m	4.72	3.47	0.50
6 m	4.88	4.09	0.71
8 m	4.29	3.67	0.60
Petzold	3.86	2.52	0.14

Discussion

The shape of the normalized VSF is variable in space and in time. The important question is whether it is possible to reduce these observations to define and bound the forms in some useful way. The normalized small-angle VSF can be expressed in a power series:

$$log(\beta) = a_0 + a_1\zeta + a_2\zeta^2 \tag{16}$$

where

$$\zeta = \ln(\theta); \quad |\theta < 20^0|$$

These simple forms describe observed data, as well as the Petzold phase function sufficiently accurately that higher-order terms are not necessary. For example, the error in fitting such a form to the Petzold phase function is everywhere $<5\%$. The coefficients that fit the observations at the four depths are shown in Table 1. The coefficients in the table nearest the surface match closely with Petzold's, but depart significantly at depth. These data emphasize the need to make observations in this region for obtaining meaningful input to models.

The ~120,000 measurements of the normalized VSF taken at the LEO-15 site in 2001 indicate that the small-angle VSF is highly variable. The normalized VSF, a close substitute of the phase function, sometimes matches Petzold's form but at other times departs significantly. The observed form does not correlate with the beam-attenuation coefficient, which is more readily measured. This lack of correlation makes it unreasonable to use a specific observed form of VSF in conjunction with readily made observations. The shape of the normalized VSF was not correlated with surface forcing by wind stress. Most importantly, there is indication of mixing of the surface and bottom layers (Fig. 5) during the 1-week period of these observations, which further complicates the search for a variable that might suggest a particular form. Ultimately, as the VSF is determined by the size distribution of particles, particle dynamics are probably the best primary information for selecting or synthesizing usable VSFs at any particular location. This work includes a power law form of the time-averaged normalized VSF at four different depths. However, the VSF is so widely variable in the field that local observations are likely required to obtain accuracy better than simply an order of magnitude.

References

AGRAWAL, Y. C., AND H.C. POTTSMITH. 2000. Instruments for particle size and settling velocity observations in sediment transport. Mar. Geol. **168:** 89–114.

BOGUCKI, D., J.A. DOMARADZKI, D. STRAMSKI, AND J. R.V. ZANEVELD. 1998. Comparison of near-forward light scattering on oceanic turbulence and particles. Appl. Optics **37:** 4669–4677.

HIRLEMAN, E. D. 1987. Optimal scaling of the inverse Fraunhofer diffraction particle sizing problem: the linear system produced by quadrature. Particle Characterization **4:** 128–133.

LEE, M. E., AND M. R. LEWIS. 2003 A new method for the measurement of the optical volume scattering function in the upper ocean. J. Atmos. Oceanic Technol. **20:** 563–571.

MOBLEY, C. M. 1994. Light and water. Academic Press.

PETZOLD, T. J. 1972. Volume scattering function for selected ocean waters. SIO Ref. 72–78.

SCHOFIELD, O., T. BERGMANN, J. KOHUT, AND S. A. GLENN. 2001. Coastal ocean observatory for studying nearhsore coastal processes. Backscatter **12:** 34–37.

SLADE, W., JR., E. BOSS, AND L. AZEVEDO. 2004. Calibration of the LISST-100 to provide near-forward volume scattering function. *In* Ocean Optics XVII, Proceedings SPIE Conference on Ocean Optics, 25–29 October, Fremantle, Australia.

VAN DE HULST, H. C. 1981. Light scattering by small particles. Dover Publications.

VOSS, K. J. AND R. W. AUSTIN. 1993. Beam attenuation measurement error due to small-angle scattering acceptance. J. Atmos. Ocean Technol. **10:** 113–121.

ZHANG, X., M. LEWIS, M. LEE, B. JOHNSON, AND G. KOROTAEV. 2002: The volume scattering function of natural bubble populations Limnol. Oceanogr. **47:** 1273–1282.

Received: 29 April 2004
Accepted: 5 June 2005
Amended: 10 July 2005